

A Sample of IRAS Infrared-Selected Seyfert 1.5 Galaxies: Infrared-Color $\alpha(60, 25)$ Dominated Eigenvector 1

J. Wang and J. Y. Wei

National Astronomical Observatories, Chinese Academy of Sciences, Beijing, China

wj@bao.ac.cn

and

X. T. He

Department of Astronomy, Beijing Normal University, Beijing, China

ABSTRACT

The well-documented E1 relationships are first extended to infrared color $\alpha(60, 25)$ and flux ratio $[\text{OIII}]/\text{H}\beta_n$ by comparing emission line properties to continuum properties in infrared wavelength. Both direct correlations and a principle component analysis are used in a sample of 50 IRAS IR-selected Seyfert 1.5 galaxies. In addition to confirm the correlations of E1 in Boroson & Green (1992), our Eigenvector 1 turns out to be dominated by mid-infrared color $\alpha(60,25)$, and most strongly effected by RFe, $[\text{OIII}]/\text{H}\beta_n$, and $\text{EW}(\text{H}\beta_b)$. Our analysis indicate that the objects with large E1 tend to co-existent with relatively young nuclear stellar populations, which implies that the E1 is related with nuclear starformation history. The IR-dominated Eigenvector 1 can be, therefore, inferred to be interpreted as “age” of AGN. In confirmation of Xu et al. (2003), it is clear that the extreme Seyfert galaxies with both large RFe and large $[\text{OIII}]/\text{H}\beta_n$ are rare in our Universe.

Subject headings: Galaxies: Seyfert – Quasars: emission lines – infrared: galaxies

1. Introduction

In order to understand the basic properties underlying the observed AGN’s spectra, a number of consistent correlations among the observational parameters have been explored.

Among these properties, the Eigenvector 1 (E1) introduced by Boroson & Green (1992, hereafter BG92) is a milestone. These authors examined the properties of a sample of 87 bright Palomar-Green (PG) quasars and found from a principal component analysis (PCA) that the E1 correlates with the strength of FeII and anti-correlates with the strength of the [OIII] line emission. Up to date, the best E1 correlation space involves (1) RFe, defined as flux ratio between the FeII complex and $H\beta$, and (2)FWHM of $H\beta$ broad component, supplemented by (3) soft X-ray photon index, Γ_{soft} (e.g. Wang et al. 1996; Sulentic et al. 2000a; Xu et al. 2003; Sulentic et al. 2002; Grupe 2004, Laor et al. 1997; Lawrence et al. 1997; Grupe et al. 1999; Vaughan et al. 2001; Sulentic et al. 2004).

At present, a great deal of evidence suggests that the Eddington ratio, defined as L/L_{Edd} , is the principle physical driver of E1 (e.g. Sulentic et al. 2000a,b; Boroson 2002; Xu et al. 2003; Grupe 2004; Marziani et al. 2003b; BG92). Moreover, Marziani et al. (2001) reproduced an artificial relationship between RFe and FWHM of $H\beta$, the strongest anti-correlation in E1 space, by combining some observational and numerical simulation results. In their process, the relation can be interpreted as driven by L/L_{Edd} associated with central black hole mass. The evolutionary significance of E1 was suggested that it might represent the “age” of AGN (Grupe et al. 1999; Grupe 2004). Narrow-Line Seyfert 1 galaxies (NLS1s) with large L/L_{Edd} and small black hole mass might be young AGNs with more activity and in their earlier evolution phase (Mathur 2000).

Over past few years there have been remarkable developments in understanding of connection between AGN and star formation in their host galaxies. A tight correlation between the mass of the black hole and the mass of galactic bulge within which it resides has been firmly established in past decade (e.g. Ferrarese & Merritt 2000; Gebhardt et al. 2000; Marconi & Hunt 2003; Magorrian et al. 1998; Richston et al. 1998; Tremaine et al. 2002). On the basis of this correlation many investigations indicated that there might be a close connection between the formation of the black hole and that of its host galaxy (Heckman et al. 2004 and references therein).

If the black hole co-evolves with galactic bulge, and If the E1 is related with the “age” of AGN as suggested by Grupe (2004), it is logically expected that the nuclear stellar population is related with the E1 correlations. This relationship could be directly examined by investigating the nuclear stellar populations by optical stellar absorption features (most notably the Balmer series and HeI lines) in broad line AGNs. In fact, so far a few attempts to detect the nuclear stellar features in type I AGNs have been made. Canalizo & Stockton (2001) investigated the age of nuclear stellar populations in the host of nine nearby QSOs by detection of Balmer absorption lines in the surrounding of the QSO or nebular HII emission lines. The estimated ages range from a few Myr old to poststarburst ages.

Brotherton et al. (1999) identified a stellar component with 400 Myr old instantaneous starburst in quasar UN J1025-0040. An exact Balmer jump was recently identified in NLS1 SDSS J022119.84+005628.4 (Wang et al. 2004). Zhou et al. (2005) recently compiled a sample of 74 poststarburst type I AGNs from Sloan Digital Sky Survey (SDSS). All these studies attempting to detect nuclear stellar population have been limited to a few particular AGNs or poststarburst galaxies (approximately 1 Gyr old starbursts) with very deep Balmer absorptions and prominent Balmer jump. However, a systematic spectroscopic study of circumnuclear stellar population of a large type I AGN sample have been damped by the difficulty in degenerating AGN and its host galaxy. Because both broad emission lines and AGN continuum mask the stellar features at optical band, the detection of absorption lines of young stars at optical wavelength is usually quite difficult in most of Seyfert 1 galaxies or quasars.

The question of the nuclear stellar population can be approached in an alternative way. The far-infrared warmth as quantified by the $\alpha(60,25)$ index¹ has been usually used as an important tool to discriminate AGN and starburst activity in the nuclear or circumnuclear regions of galaxies (de Grijp et al. 1985; Lipari 1994; Barthel 2001). Because of additional heating input from the hard continuum radiation of central active nucleus, AGNs have warmer dust than do starburst regions (e.g. Low et al. 1988). The color $\alpha(60,25)$, therefore, allows us to address the relative importance of AGN-activity and starburst-activity in not too distant active galaxies (see section 4.1 for details). In this paper, we will use the infrared colors adopted from the IRAS survey to extend the well-known E1 relationships to AGN's infrared properties.

There is another goal of this paper. Recently, a new relationship between flux ratio of [OIII] to $H\beta$ narrow component and flux ratio of optical FeII blends to $H\beta$ broad component was found in an AGN sample with high X-ray to optical flux ratio from ROSAT All-Sky Survey (RASS) (Xu et al. 2003). In their analysis, there were always large uncertainties in determining the fraction of $H\beta$ emitting from the NLR. Deblending the optical permitted lines in a majority of cases is difficult because no transition between the narrow and broad components is observed. The anti-correlation between flux ratios FeII/ $H\beta_b$ and [OIII]/ $H\beta_n$ should be, therefore, investigated again and verified by involving a sample of Seyfert 1.5 galaxy (Osterbrock 1989, Winkler 1992). Intermediate-type Balmer emission profile allows us to accurately extract narrow $H\beta$ component from the integrated profile of emission line.

In this paper, we examine the properties of optical emission lines of 50 bright Seyfert 1.5

¹The infrared color index $\alpha(\lambda_1, \lambda_2)$ is defined as $\alpha(\lambda_1, \lambda_2) = -\frac{\log[F(\lambda_2)/F(\lambda_1)]}{\log(\lambda_2/\lambda_1)}$, where the wavelengths are in units of μm .

galaxies and discuss their connection with infrared colors. These nearby AGNs were selected from the Catalog of quasars and active nuclei: 10th edition (Veron-Cetty & Veron 2001) and the Catalog of the the IRAS Survey. Both direct correlations and PCA method are used to analyze the observed properties.

The paper is organized as follows. The observational information and detailed spectral measurements are given in §2. The statistical properties are investigated in §3. Several diagnostically important correlations are studied. We discuss the implications of the results in §4. A brief summary of main conclusions of this paper is given in the final section. A cosmology with cosmological constant: $\Omega_m = 0.3$, $\Omega_\Lambda = 0.7$ and $h_0 = 0.7$ is adopted for luminosity calculations.

2. Observations and Emission Lines Measurements

The sample of objects was compiled from the Catalog of quasars and active nuclei: 10th edition (Veron-Cetty & Veron 2001) and IRAS survey. Because of the constraint of the observatory site and instrumental capability, the objects were selected by requiring the objects to be in the northern sky ($\delta > -10^\circ$) and to be optical bright ($m_v \leq 16.0$ mag). Specially, there are total 66 such objects listed in Veron-Cetty & Veron (2001). Seven of the objects were not observed because of the poor weather conditions.

Total 59 high quality spectra were obtained by using NAOC 2.16m telescope in Xinglong observatory during several observing runs performed from November 2001 to October 2004. The observations were carried out by OMR spectrograph, using a Tektronix 1024×1024 CCD as detector. Two sets of spectra, denoted as set A and B, were involved in final emission lines measurements. For each object, the observation was performed with either set A or B. The set A spectra were taken with a grating of 300 g mm^{-1} and a slit of $2''$ oriented in south-north direction. This setup provided a spectral resolution $\sim 10 - 11 \text{ \AA}$ as measured from comparison spectra. The observations of set B spectra with a resolution of $\sim 5 - 6 \text{ \AA}$ were performed with a grating of 600 g mm^{-1} and a slit of $2.5''$ oriented in south-north direction. The blazed wavelengths were 6000 \AA and 5400 \AA in set A and B spectra, respectively. Generally, the setup in set A provided a wavelength coverage of $3800 - 8700 \text{ \AA}$ in observed frame. This attempt covered both $H\beta$ and $H\alpha$ region in a single exposure in almost all set A spectra, except objects CSO 409, 3C 351 and 3C 48.0, because of their large redshifts. On the other hand, only $H\beta$ region, from 4200 \AA to 6600 \AA in observed frame, was covered in set B spectra. Exposure time was generally between 600-3600 seconds depending on the brightness of the object. In a majority of the observations, each object was exposed successively twice. The two frames were combined prior to extraction to enhance the S/N ratio and eliminate the

contamination of cosmic-ray easily. The wavelength calibration associated with each object was carried out by helium-neon-argon comparison arcs obtained at the position being nearly identical to that of particular object. Two or three KPNO standard stars (Massey et al. 1988) were observed per night both for performing flux calibration and for the removal of atmospheric absorption features. All the objects were observed as close to meridian as possible.

In our final spectral data set, we find that the spectra of five out of 59 objects are contaminated strongly by spectra of their host galaxies. In addition, there were no obvious broad $H\beta$ component (with no or very faint $H\alpha$) in other four objects. These 9 objects are finally excluded from our spectral measurements and from finally statistical analyses. The log of observations of remaining 50 objects is given in Table 1.

The unprocessed frames were reduced in standard procedures using IRAF package. The CCD reductions included bias subtraction, flatfield correction, and cosmic-ray removal before sign extraction. One-dimensional sky-subtracted spectra were wavelength and flux calibrated. For each of the standard stars, the observed flux at wavelength 5000\AA was compared to its absolute flux. This procedure roughly yields that the uncertainty of the flux calibration is generally no larger than 20%. The Galactic extinctions were corrected by color excess, parameter $E(B-V)$ from NED, assuming an $R_V = 3.1$ extinction law (Cardelli et al. 1989). The spectra were transformed to rest frame, along with K-correction, according to the narrow peak of $H\beta$.

2.1. FeII subtraction

It was long time to be known that the contamination of the FeII complex is a complicating factor in measuring strength and profile of particular emission lines such as $H\beta$, $[\text{OIII}]\lambda\lambda 4959, 5007$ and $\text{HeII}\lambda 4686$. In order to reliably measure line properties and to determine the strength of the FeII blends it is necessary to appropriately model the FeII complex. The generally accepted model is the empirical template of the FeII complex described in BG92. The FeII template is the optical FeII emission in IZW1, a bright NLS1 being of strong and narrow permitted FeII emission (Phillips 1978; Oke & Lauer 1979; Veron-Cetty et al. 2004). Briefly, the template is a two-dimensional function of line width (FWHM) and intensity of the FeII blends.

The same method described in BG92 was adopted in our measurements. The whole template is broadened to the FWHM of the broad component of $H\beta$ line by convolving with a Gaussian profile and scaled to match the line intensity. Usually, the contribution of the

FeII complex around $H\beta$ can be well removed in terms of this template. The best subtraction of the FeII complex is derived by searching in the parameter space and producing a slick continuum at blue of $H\beta$ and between 5100\AA and 5500\AA after the subtraction. The flux of the FeII complex is measured between the rest wavelength 4434\AA and 4684\AA as in BG92.

The schemes of the FeII subtraction in two typical cases 3C48.0 and II Zw1 are illustrated in Figure 1. In each panel, the observed spectrum and resulting FeII-subtracted spectrum are displayed by the upper and middle curves, respectively. Note that the observed spectra are offset upward arbitrarily for visibility. The best adopted FeII templates are shown by bottom curves.

2.2. Profile modelling and measurements of other lines

The FeII-contamination subtracted spectra are used to measure the non-FeII properties. The first step in the processing of the spectra is to remove the continuum from each object. The continuum is fitted by a power-law to the regions which seemed to be uncontaminated by emission lines. The two selected strong emission-line free windows are generally from $\lambda 4500$ to $\lambda 4600$ and between 5100\AA - 5500\AA . There are two parameters in determining each continuum component, i.e., the flux and the slope.

In our study, the observed line profiles are reproduced by a single Gaussian component and/or by a set of several Gaussian components because of their simplicity and practicability (Xu et al. 2003; Evans 1988; Rodriguez-Ardila et al. 2000). The line profiles are modelled and measured by SPECFIT task (Kriss 1996) in IRAF package. The fitting is persisted until the minimum of χ^2 , the measurement of goodness of profiling, is achieved. In each spectrum, the line profiles are modelled as follows. 1) Each of the forbidden lines [OIII] $\lambda\lambda 4959, 5007$ are modelled by a single Gaussian component. The atomic relationships, $F_{5007}/F_{4959} \doteq 3$ (Storey & Zeippen 2001) and $\lambda_{4959}/\lambda_{5007} = 0.9904$, are used to reduce the number of free parameters and to improve the reliability of fitting procedure. 2) The profile modelling of $H\beta$ line is straightforward in the spectra of objects of intermediate type. Each $H\beta$ profile is modelled by a set of two Gaussian components: a narrow and a broad Gaussian components. The broad component of $H\beta$ is referred as $H\beta_b$ and is considered as representative of the broad line region (BLR). The narrow component is referred as $H\beta_n$. This adopted procedure accords with the generally accepted unified model of AGN in which the narrow and broad $H\beta$ components are emitted from NLR and BLR, respectively.

The distribution of ratio between $\text{FWHM}(H\beta_n)$ and $\text{FWHM}([OIII])$ (both with instrumental resolution correction, see §3.1 for details) is illustrated in Figure 3. A statistical

analysis indicates that this ratio has a mean value of 1.26 and a standard deviation of 0.57. It is noted that there are a few objects in which a distinct narrow component is invisible in our sample. The interpretation of the profile de-composition should be careful, although the observed profile can be fitted with two Gaussian component adequately. Detailed examination of the results suggests that the flux of narrow $H\beta$ is generally overestimated because the $\text{FWHM}(H\beta_n)$ is much large than that of [OIII] line (e.g. 5 objects with $\text{FWHM}(H\beta_n)/\text{FWHM}([\text{OIII}]) > 2.0$). For these cases, we set the $H\beta_n$ is unavailable and set the total $H\beta$ flux as $H\beta_b$ (see also in Wang et al. 2005, Zheng et al. 2002). As described in BG92, the contribution of narrow component is rarely more than 3% of total $H\beta$ flux, even when there is a distinct narrow $H\beta$ emission.

The modelling described above works well in most objects except in a few cases, for example the objects 3C 390.3 and Mark 509. The object 3C 390.3 is a radio-loud (RL) Seyfert galaxy that shows double-peaked structure in their Balmer emission lines (e.g. O’Brien et al. 1998; Eracleous & Halpern 2003; Strateva et al. 2003). To measure the broad $H\beta$ emission of 3C 390.3, we employ two separated broad Gaussian components to reproduce the observed double-peaked profile. In 3C 390.3, the flux of $H\beta$ broad component includes the contributions of both broad Gaussian profiles. In Mark 509, a very broad $H\beta$ component ($\text{FWHM} \sim 10000 \text{ km s}^{-1}$) must be acquired to reproduce the observed profile. Generally, the very broad emission line region (VBLR, $\text{FWHM} > 7000 \text{ km s}^{-1}$) is suggested to be optically thin to Balmer ionizing continuum and located at the inner edge of classical BLR (e.g. Corbin 1997a, b; Brotherton & Wills 1994; Kuraszkiewicz et al. 2004). Sulentic et al. (2000c) reported a demise of classical BLR in luminous quasar PG 1416-129. There remained a redward asymmetric very broad emission line component. These authors suggested that the wing of $H\beta$ line are dominated by emission from optically thin VBLR. Moreover, the existence of VBLR is also supported by the observation of very broad and boxy profile of high ionized emission lines such as $\text{HeII}\lambda 4686$ (Marziani et al. 2003a).

As an illustration, the profile decomposition is shown in Figure 2 for two typical cases, MS 0412.4-0802 and IRAS 05078+1626. The observed spectra are represented by light solid lines, the modelled spectra by heavy solid lines. The narrow and broad components are shown by short and long dashed lines respectively. The lower panel underneath each spectrum illustrates the residual between the observed and modelled profiles.

3. Results and Analysis

3.1. Results and correlations

In order to investigate the statistical properties of a set of data, we list in Table 2 the following items measured from spectra. Column (2) lists the equivalent width of $H\beta_n$, and Column (3), the equivalent width of $H\beta_b$. The equivalent width of the optical FeII complex measured between rest wavelength $\lambda 4434$ and $\lambda 4634$ is listed in Column (4). All equivalent width measurements refer to the continuum level at position of $H\beta$, $\lambda 4861$. The continuum level is determined from the modelled power-law continuum. Column (5) gives the FWHM, in units of km s^{-1} of $H\beta_n$. Column (6) lists the FWHM of $H\beta_b$. The FWHM of $[\text{OIII}]\lambda 5007$ is listed in column (7). All quoted widths of emission lines were corrected for instrumental resolution. The intrinsic line widths were obtained by $\Delta\lambda_{\text{true}}^2 = \Delta\lambda_{\text{obs}}^2 - \Delta\lambda_{\text{inst}}^2$ there $\Delta\lambda_{\text{inst}}$ is the instrumental resolution that is determined from the width of night-sky emission lines and tested by the spectra of comparison lamp. The next column lists the flux ratio $[\text{OIII}]/H\beta_n$. The flux ratio, denoted as RFe, is listed in column (9). The RFe is defined as the flux ratio between the FeII complex and $H\beta_b$. The velocity shift of central wavelength of $H\beta_b$ with respect to that of $H\beta_n$ is listed in column (10). Column (11) lists the velocity shift of Gaussian peak of $[\text{OIII}]$ relative to that of $H\beta_n$. In both column (10) and (11), a positive velocity indicates a redshift of $H\beta_b$ and a redshift of $[\text{OIII}]$ line, respectively, whereas a blueshift is inferred by a negative velocity. The column (12) and (13) list the far-infrared color $\alpha(60, 100)$ and mid-far-infrared color $\alpha(60, 25)$, respectively. The luminosity of $[\text{OIII}]$ emission line is listed in the last column.

Having measured and tabulated a number of emission-line and continuum properties for this infrared selected Seyfert 1.5 galaxies sample, we proceed to determine which features are correlated. This is approached by performing a correlation analysis on the particular parameters that are measured from lines and continuum. The Spearman rank-order correlation matrix, along with its significance matrix for measured properties, is calculated. The complete correlation coefficient matrix is presented in Table 3. The probability of the null correlation, P_s , for a sample with corresponding correlation coefficient r_s is also shown in Table 3 for entries with $P_s < 0.05$. Each correlation coefficient is computed using only the objects for which both values are derived. The coefficients involving RFe are calculated by survival analysis, because the RFe with zero value is non-detectable and treated as a lower limit in statistical analysis.

3.1.1. *RFe vs. FWHM(H β_b) and RFe vs. L([OIII])*

The well-documented anti-correlation between RFe and FWHM(H β) has been confirmed in many studied AGN samples (e.g. BG92; Xu et al. 2003; Grupe 2004; Sulentic et al. 2000, 2004). It is clear that our analysis reproduces this anti-correlation which is moderately strong ($r_s = -0.321$, $P_s = 0.0279$) in our moderately large sample of type 1.5 Seyfert galaxy. This correlation is shown in the lower panel of Figure 4. BG92 found that their E1 has significant correlation with RFe and [OIII] absolute magnitude. The similar anti-correlation between strength of FeII and [OIII] strength has also been detected by many authors (e.g. Zheng et al. 2002; Vaughan et al. 2001). In the present data, we detected a relatively strong ($r_s = -0.386$, $P_s = 0.0081$) anti-correlation between RFe and [OIII] luminosity. The upper panel of Figure 4 illustrates this correlation.

3.1.2. *Correlations with IR color index $\alpha(60,25)$*

In addition to confirm the E1 correlations in BG92, newly discovered correlations involving the IR color index $\alpha(60,25)$ are found in our sample. These correlations are displayed in Figure 5. Figure 5(a) displays the anti-correlation between the $\alpha(60,25)$ and RFe. The anti-correlation is strong ($r_s = -0.518$, $P_s = 0.0003$) in the present data whereas it is only weak ($r_s = -0.140$) if the color is compared directly with EW(FeII). This means that the correlation between $\alpha(60,25)$ and RFe arises because EW(H β_b) gets larger as the mid-infrared warmth gets hotter. The correlation between $\alpha(60,25)$ and [OIII]/H β_n is plotted in Figure 5(b). The calculated correlation coefficient is $r_s = -0.538$, corresponding to a significance level $P_s = 0.0012$. This plot shows a trend for the objects with higher ratio [OIII]/H β_n to have hotter mid-infrared warmth. The similar correlation is found by Keel et al. (1994) in a large sample of “warm” Seyfert 2 galaxy. The correlation between $\alpha(60,25)$ and EW(H β_b) is illustrated in Figure 5(c). A Spearman rank-order test yields a correlation coefficient $r_s = 0.590$ ($P_s < 10^4$). In Figure 5(c), the lower the value of EW(H β_b), the cooler the mid-far-infrared color. The strong ($r_s = 0.478$, $P_s = 0.0009$) correlation between $\alpha(60,25)$ and $L([OIII])$ is illustrated in Figure 5(d). When the mid-infrared warmth increases, the luminosity of [OIII] line increases.

3.2. Principle component analysis

In fact, some significant relations are due to selection effects and the fact that we have chosen to measure essentially the same properties in somewhat different ways (see e.g. BG92;

Xu et al. 2003; Grupe 2004). The correlation between $EW(\text{FeII})$ and $R\text{Fe}$ ($r = 0.692, P_s < 10^{-4}$) are due to dependent parameters. In addition, the correlations between different measures of same property (e.g. $EW(\text{H}\beta_b)$ and $R\text{Fe}$) and another property (e.g. $\alpha(60, 25)$) are degenerated. To investigate the correlations more meaningfully, we perform a PCA on the correlation matrix. The PCA is applied to 36 out of 49 objects using the following eight parameters: the $EW(\text{H}\beta_b)$, parameter $R\text{Fe}$, FWHM of $\text{H}\beta_b$, flux ratio $[\text{OIII}]/\text{H}\beta_n$, $\Delta V(\text{H}\beta)$, $\Delta V([\text{OIII}])$, infrared colors $\alpha(60, 100)$ and $\alpha(60, 25)$, and $L[\text{OIII}]$ each of which contains potentially unique information. The Spearman (rank-order) correlation matrix is used to run PCA program. Rank values are used rather than the measured properties, because the influence of extreme objects can be minimized by this nonparameter analysis (Brotherton 1996).

Table 4 shows the results of PCA. The first four components together account for marginally more than 70% of the variance, and the first principle component seems to be an important underlying parameter that governs the observed properties of the AGN. The PCA indicates that the first principle component is dominated by mid-infrared color $\alpha(60, 25)$. It has a projection -0.841 on the Eigenvector 1 while the next high projection is only 0.224 on Eigenvector 4. In addition, the Eigenvector 1 has a strong effect on $R\text{Fe}$, $[\text{OIII}]/\text{H}\beta_n$, and $EW(\text{H}\beta_b)$. Other three properties, $\text{FWHM}(\text{H}\beta_b)$, $\Delta V([\text{OIII}])$ and $L([\text{OIII}])$, are also correlated with Eigenvector 1.

3.3. Other properties

Figure 6(a) displays the anti-correlation between the $\Delta V([\text{OIII}])$ and $\text{FWHM}(\text{H}\beta_b)$ ($r_s = -0.343, P_s = 0.0230$). There is a trend that objects with wider $\text{H}\beta$ line tend to have larger velocity shift of $[\text{OIII}]$ with respect to the $\text{H}\beta$ narrow component. The correlation between the $\Delta V([\text{OIII}])$ and $R\text{Fe}$ is shown in Figure 6(b) ($r_s = -0.320, P_s = 0.0319$).

Xu et al. (2003) reported a significant ($r_s = 0.600, P_s < 10^{-4}$) anti-correlation between the $R\text{Fe}$ and flux ratio $[\text{OIII}]/\text{H}\beta_n$ by investigating an AGN sample with high X-ray-to-optical flux ratio from RASS. Our statistical analysis indicates that this correlation is weak in our sample, however. The lack of strong correlation in our sample is most likely due to under-sampling. Figure 7 is plot of the $R\text{Fe}$ vs. flux ratio $[\text{OIII}]/\text{H}\beta_n$ for our sample ($r_s = -0.252$) and sample in Xu et al. (2003). The data presented in this paper are marked with solid squares, and Xu et al. (2003) sample with open triangles.

Although the correlation in our sample is not as strong as that obtained by Xu et al. (2003), we find that the point distribution of our sample is similar to that shown by Xu et

al. (2003). The digram is not evenly populated for both two samples. It is clear that almost all the objects in two samples are predominately found in the region being under a solid line drawn by eye, and the extreme region with large RFe and large flux ratio of [OIII] to $H\beta_n$ is restricted.

The distribution of the line flux ratio $[OIII]/H\beta_n$ of the objects in our sample is displayed in Figure 8. We find a mean value of 7.02 and a standard variance of 3.58. Generally, the characteristic ionization state of gas photoionized by the Seyfert 1 nucleus is of very high $[OIII]/H\beta_n \sim 10$. However, very low ionized NLR can be identified in a fraction of the objects in our sample. For 36 objects with measured flux ratio $[OIII]/H\beta_n$ in our sample, there are 5 objects (i.e. 1H 1934-063; IRAS 00580+3055; MCG +08-11-011; MCG +08-15-056; NMP1G 05.0216) with $[OIII]/H\beta_n < 3$. It indicates that these 5 objects can not entirely classified as Seyfert 2 galaxies when their BLR are obscured by the torus on the line-of-sight (Veilleux & Osterbrock 1987). As discussed below, there are two most likely interpretations of these extremely small ratio of $[OIII]/H\beta_n$: [OIII] suppression due to high density as suggested by Xu et al. (2003) and contamination of starburst.

4. Discussion

4.1. Connection between Eigenvector 1 and nuclear starformation history

It is noted that an eigenvector is always specific to a certain sample depending on which observed parameters have been used and the range of parameters. There is, therefore, no one “Eigenvector 1” for every AGN sample. In our infrared-selected Seyfert 1.5 galaxies sample, the Eigenvector 1 is dominated by mid-infrared color $\alpha(60, 25)$. The most prominent correlations indicates the trends for objects with “cold” mid-infrared color to have small flux ratio $[OIII]/H\beta_n$, small $EW(H\beta_b)$, low luminosity of [OIII], and large value of RFe.

The understanding of role of the infrared color $\alpha(60, 25)$ is not straightforward. Generally, the infrared color $\alpha(60, 25)$ allows us to determine the relative importance of AGN-activity and starburst-activity in a galaxy. Low et al. (1988) pointed out that in many cases AGNs display a warmer dust than do starforming regions. This warmer dust is heated by an additional heating caused by an intense radiation emitted from the nucleus, and strongly influence the mid-infrared flux at $25\mu\text{m}$. De Grijp et al. (1985) reported that the infrared color $\alpha(60,25)$ can be used as an efficient parameter to discriminate AGN and starburst activity in the nuclear and circumnuclear regions of galaxies. A high fraction of Seyferts among galaxies can be obtained with $\alpha(60, 25) > -1.5$. Kewley et al. (2001) assessed the relative importance of AGN- and starburst-activity in type II AGN by combining the infrared color with line

ratio $[\text{OIII}]/\text{H}\beta_{\text{n}}$. They found that the AGNs have on average a warmer infrared color than starbursts. Hao et al.(2005) indicated that the infrared selected QSOs with significant far-IR excess contributed by starburst have smaller color index $\alpha(60, 25)$. As additional evidence, Gonzalez Delgado et al. (2001) found that, in Seyfert 2 galaxies, the nuclei with young and intermediate-age population show lower ionization level (smaller flux ratio $[\text{OIII}]/\text{H}\beta_{\text{n}}$) and cooler $\alpha(60,25)$ than the nuclei dominated by an old stellar population. When the relative importance of starburst increases, our results indicate that the $\text{FeII}/\text{H}\beta_{\text{b}}$ ratio increases, and $\text{EW}(\text{H}\beta_{\text{b}})$, $[\text{OIII}]/\text{H}\beta_{\text{n}}$ and $L([\text{OIII}])$ decrease.

The far-infrared color-color diagram has been generally used as an efficient tool to discriminate between different types of activity in the nuclear and circumnuclear starforming region of galaxies. As an additional test, the IRAS infrared color-color diagram is shown in Figure 9. In the same diagram, the power-law line is also indicated. The AGN and starburst loci are shown by short and long dashed lines, respectively. The AGN locus is adopted from Canalizo & Stockton (2001), and the starburst locus from Lipari (1994, and references therein). The size of each point is proportional to the projection on Eigenvector 1 of the corresponding object. It is noted from Figure 9 that the objects with small projection on Eigenvector 1 are mainly located in QSO/Seyfert region, while the objects showing large projection are distributed in/near the starburst region.

Some comments on the objects located in/near the starburst region are discussed more detailed as follows:

- *3C 48.0*, This object displays morphological evidence for a recent merger event with a likely double nuclei and a tidal tail extending several arcseconds (Canalizo & Stockton 2000, Stockton & Ridgway 1991, Chatzichristou et al. 1999). Very young stellar populations were suggested in the second nucleus about 1" northeast of the QSO (Canalizo & Stockton 2000). Recent near infrared observations of the second nucleus indicated the presence of warm dust that is likely heated by starbursts or ongoing starformation (Zuther et al. 2004).
- *NGC 3227*, This object is a nearby Seyfert galaxy interacting with a gas-poor companion. A clear $3.3\mu\text{m}$ polycyclic aromatic hydrocarbon (PAH) emission feature, which is usually associated with starformation activity, was identified in its inner 60pc ($\text{EW}_{3.3} = 52 \pm 10\text{\AA}$, Rodriguez-Ardila & Viegas 2003). These authors also observed another two objects: Mark 766 and 1H 1934-063 that are listed in our sample. In Mark 766, the PAH feature has been detected as well ($\text{EW}_{3.3} = 40 \pm 11\text{\AA}$), while no evidence for PAH feature has been observed in 1H 1934-063 ($\text{EW}_{3.3} < 10\text{\AA}$). The position of 1H 1934-063 in the color-color diagram is indicated by an open star. As a

first inspection, both NGC 3227 and Mark 766 have much cooler $\alpha(60, 25)$ than does 1H 1934-063.

- *NGC 7469*, This object is an luminous infrared source. Its circumnuclear ($1''.5-2''.5$) ring structure has been observed at radio, optical, near-infrared, and mid-infrared bands (see references in Davies, Tacconi & Genzel 2004). Using the $2.3\mu\text{m}$ CO 2-0 absorption and continuum slope, Davies, Tacconi & Genzel (2004) resolved the nuclear star cluster ($0''.15-0''.20$) and found that the age of the cluster is less than about 60 Myr.
- *Mark 732*, Cid Fernandes et al. (1998) obtained the spatial resolved long slit spectra of this object. Circumnuclear young stellar features are identified in the spectrum of region being north-east of the nucleus ($4''$ away from the nucleus).

In summary, in our IR-selected AGN sample, the Eigenvector 1 not only holds the correlations appeared in BG92’s E1, but also first extends the well-documented E1 space into infrared color $\alpha(60, 25)$ and ratio $[\text{OIII}]/\text{H}\beta_{\text{n}}$. This extension suggests that the E1 relates with nuclear starformation history, and that the E1 can be interpreted as “age” of AGN as suggested by Grupe (2004). When the Eigenvector 1 increases, AGN with larger RFe tends to co-existent with relatively young stellar populations.

Both observational evidence and theoretical scenario indicate that starburst is a key piece of the AGN machinery through evolutionary processes. The understanding of co-existence of AGN and star formation in their host galaxies is accumulating. Powerful circumnuclear starbursts ($< \text{Gyr}$) have been unambiguously identified in $\sim 40\%$ of nearby Seyfert 2 galaxies by several optical spectroscopic investigations of moderately large samples of type 2 Seyfert nuclei (e.g. Joguet et al. 2001; Gonzalez Delgado, Heckman & Leitherer 2001; Cid Fernandes et al. 2001, Storchi-Bergman et al. 2001). Gonzalez Delgado (2002) summarized the evidence in favor of the co-existence of AGN and starburst activity by showing the observations at optical and near-infrared band. Theoretical studies also provided a plausible picture about the co-evolution of AGN and circumnuclear starburst (e.g. Granato et al. 2004). In the early phase of AGN development, the star-formation rate is high, which means there are plenty of gases that can be attracted into the nucleus of galaxy under the gravitation of the central black hole. These gases are ultimately accreted onto black hole and lead to a high accretion rate. At latter phase, the accretion rate decreases because of the diminishing of content of gas.

PCA is a quantitative method for replacing a group of variables with a new variable. This group of variables might be generally measuring the same driving principle.

Generally, the ratio $[\text{OIII}]/\text{H}\beta_n$ (and also $L([\text{OIII}])$) is orientation independent because both lines are emitted only from optically thin region at large enough distance from the nucleus to be unobscured by the material causing the anisotropy in the featureless nuclear continuum and in the broad lines (Jackson et al. 1989). The isotropy of $[\text{OIII}]$ line emission has been questioned by some studies of radio-loud AGNs (Baker 1997; di Serego Alighieri et al. 1997). However, the correlation between $[\text{OIII}]$ and orientation independent $[\text{OII}]$ emission indicates that the $[\text{OIII}]$ emission is not dependent on orientation effect (Kuraszkiewicz 2000). The mid-far-infrared color is also a nominally unbiased isotropic property. It is a reasonable first approximation, although this may not be strictly true if the torus is optically thick in the mid-infrared (e.g. Pier & Krolik 1992; Granato & Danese 1994). On the basis of these results, it is not likely that the correlations in our Eigenvector 1 is only due to the orientation effect.

At present, the E1 is mostly interpreted as governed by L/L_{Edd} (e.g. Boroson 2002; Grupe 2004). It is, therefore, reasonable to expect that our Eigenvector 1 is most possibly driven by L/L_{Edd} as well. The parameter RFe is usually considered as a good tracer of L/L_{Edd} (BG92; Boroson 2002; Marziani et al. 2001; Zamanov & Marziani 2002, Netzer et al. 2004) and scales with L/L_{Edd} as $\text{RFe} \propto 0.55 \log(L/L_{\text{Edd}})$ (Marziani et al. 2001). If so, the anti-correlation between RFe and mid-far-infrared color $\alpha(60,25)$ possibly reveals a linkage between L/L_{Edd} and nuclear starformation history, and that L/L_{Edd} is large in AGN with relatively strong starburst-activity (e.g. Hao et al. 2005). In order to test this scenario, L/L_{Edd} and black hole mass are necessary to be calculated. This calculation is, however, not convincing in our Seyfert 1.5 sample, because of the influence of orientation effect which obscures a large fraction of continuum emitting from the central engine. The role of L/L_{Edd} will be tested in the next work by a larger sample of type I AGN .

On the basis of above discussions, we further conjecture that the correlation between RFe and $\alpha(60,25)$ implies an evolutionary trace of Seyfert galaxies and QSOs. Cid Fernandes et al. (2001) speculated that the composite starburst plus Seyfert 2 nucleus system evolve into pure Seyfert 2 galaxies. As analogue with the evolutionary scenario of Ultra infrared luminous galaxies (ULIGs) suggested by Sanders et al. (1988; see also in Hao et al. 2005 and references therein), we suspect that the “cold” Seyfert galaxies possibly evolve into “warm” Seyfert galaxies.

4.2. RFe- $[\text{OIII}]/\text{H}\beta_n$ space

As shown in §3.2, both our sample and the sample in Xu et al. (2003) show that the Seyfert galaxies are not uniformly populated in the digram plotted as $[\text{OIII}]/\text{H}\beta_n$ vs. RFe. We

note that there are significant number of objects with very small $[\text{OIII}]/\text{H}\beta_{\text{n}}$ for the sample of Xu et al. (2003). This phenomenon, however, does not appear in our sample. These very low $[\text{OIII}]/\text{H}\beta_{\text{n}}$ might be caused by the overestimate of $\text{H}\beta_{\text{n}}$ component as described in §1. Xu et al. (2003) speculated that the anti-correlation between $[\text{OIII}]/\text{H}\beta_{\text{n}}$ and RFe is mainly driven by density effect. Although this explanation can not be proved or excluded by our analysis in current data set, we propose that the contamination of starforming can also be a possible interpretation. In fact, as shown in §3.1, both $[\text{OIII}]/\text{H}\beta_{\text{n}}$ and RFe are tightly correlated with $\alpha(60, 25)$. When RFe is large, the increased relative importance of starburst could reduce the observed value of $[\text{OIII}]/\text{H}\beta_{\text{n}}$.

4.3. Outflows: a clue of linkage between BLR and NLR

The detection of $[\text{OIII}]$ velocity shift is difficult to be doubted for following two reasons: 1) in a majority of cases, the resulting wavelength accuracy is better than 1\AA . The corresponding uncertainty of velocity is less than 100 km s^{-1} ; 2) the narrow components of $\text{H}\beta$ can be modelled accurately because of the apparent profile inflection.

Zamanov et al. (2002) found that the large $[\text{OIII}]$ blueshift relative to $\text{H}\beta_{\text{n}}$ ($\Delta V([\text{OIII}]) > 250\text{ km s}^{-1}$) is confined to sources with $\text{FWHM}(\text{H}\beta_{\text{b}}) \leq 4000\text{ km s}^{-1}$. These authors interpreted the large blueshift of $[\text{OIII}]$ with respect to $\text{H}\beta_{\text{n}}$ as a result of outflow whose origin is considered to be strong radiation pressure due to large L/L_{Edd} . Their purely kinematical model suggested that the $[\text{OIII}]\lambda 5007$ blueshifts are associated with the high-ionization outflow generated in objects with high accretion rate. Many theoretical studies suggested that a high L/L_{Edd} is prefer to result in strong mass outflow. King & Pounds (2003) proposed a model in which winds in quasars are probably produced when the black holes accrete at or above the Eddington limit. The dynamical model of accretion disk wind indicates that the vertical outflow ratio strongly depends on the accretion rate. The magnitude of outflow increases significantly with the accretion rate, assuming a constant viscosity parameter (Witt, Czerny & Zycki 1997). The simplest, and mostly possible, interpretation of the correlation between $[\text{OIII}]$ shift amplitude $\Delta V([\text{OIII}])$ and RFe is, therefore, that we are clear seeing a dynamical linkage between the outflow of emission material and central accretion power in terms of a relatively strong wind arising from the central region of AGN.

5. Conclusions

This paper presents the statistical study of optical emission-line properties of a sample of 50 Seyfert 1.5 galaxies. The line properties are compared with their continuum properties in infrared wavelength to extend the documented E1 relationships into infrared property of AGN. The statistical analysis allows us to draw following conclusions:

1. We first extend the E1 relationships into infrared color $\alpha(60, 25)$ and flux ratio $[\text{OIII}]/\text{H}\beta_{\text{n}}$. In addition to confirm the BG92's E1, the PCA analysis indicates that our Eigenvector 1 is dominated by mid-far-infrared color $\alpha(60,25)$. The color $\alpha(60,25)$ is found to be strongly anti-correlated with RFe ($r_s = -0.518; P_s = 0.0003$), and correlated with EW(H β) ($r_s = -0.590; P_s < 10^{-4}$), $[\text{OIII}]/\text{H}\beta_{\text{n}}$ ($r_s = 0.538; P_s = 0.0012$), and $L([\text{OIII}])$ ($r_s = 0.478; P_s = 0.0009$). The Eigenvector 1 is inferred to increase with relative importance of starburst with respect to AGN activity, and to be, therefore, related with nuclear starformation history. We further suspect that a “cold” Seyfert galaxy perhaps evolves into a “warm” one.
2. Although the relationship between RFe and $[\text{OIII}]/\text{H}\beta_{\text{n}}$ in our sample is not as significant as that obtained by Xu et al. (2003), the populations of points are same for both our sample and Xu et al (2003). It is clear that almost all the objects are located below an envelope. This effect implies that Seyfert galaxies rarely have both large value of RFe and large ratio of $[\text{OIII}]/\text{H}\beta_{\text{n}}$.
3. Other two correlations, FWHM(H β_{b}) vs. $\Delta V[\text{OIII}]$ and RFe vs. $\Delta V[\text{OIII}]$, are identified in our sample. According to the simple kinematic model, these two correlations could provide a direct linkage between BLR and NLR.
4. In our sample $[\text{OIII}]/\text{H}\beta_{\text{n}} < 3$ are identified in 5 out of 36 objects with determined narrow component of H β . These five objects can not be classified as Type 2 AGNs when their BLR are obscured on the line-of-sight.

We are grateful to Profs. Todd A. Boroson and Richard F. Green for providing us the FeII template. We thank an anonymous referee for many useful suggestion and his careful and critical review, D. W. Xu, C. N. Hao, Y. M. Mao for valuable discussion and help. Special thanks go to the staff at Xinglong observatory as a part of National Astronomical Observatories, China Science Academy for their instrumental and observational help. This research has made use of the NASA/IPAC Extragalactic Database (NED), which is operated by the Jet Propulsion Laboratory, Caltech, under contact with the National Aeronautics and

space Administration. This work was supported by NFS of China (Grant number: 19990754, 10473013 and 10503005).

REFERENCES

- Baker, J. C., 1997, MNRAS, 286, 23
- Baldwin, J. A., 1977, ApJ, 214, 679
- Barthel, P., 2001, New A Rev., 45, 591
- Boroson, T. A., 2002, ApJ, 565, 78
- Boroson, T. A., & Green, R. F., 1992, ApJS, 80, 109
- Brotherton, M. S., Wills, B. J., 1994, A&AS, 184, 6003
- Brotherton, M. S., van Breugel, Wil, Stanford, S. A., 1999, ApJ, 520, 87
- Canalizo, G., & Stockton, A., 2000, ApJ, 528, 201
- Canalizo, G., & Stockton, A., 2001, ApJ, 555, 719
- Cardelli, J. A., Clayton, G. C., & Mathis, J. S., 1989, AJ, 345, 245
- Chatzichristou, E. T., Vanderriest, C., & Jaffe, W., 1999, A&A, 343, 407
- Cid Fernandes, Heckman, T., Schmitt, H., Gonzalez Delgado, R. M., Storchi-Bergmann, T., 2001, ApJ, 558, 81
- Cid Fernandes, R., Storchi-Bergmann, T., & Schmitt, H. R., 1998, MNRAS, 297, 579
- Corbin, M., 1997a, ApJS, 113, 245
- Corbin, M., 1997a, ApJ, 532, 136
- Davies, R. I., Tacconi, L. J., & Genzel, R., ApJ, 602, 148
- de Grijp, M. H. K., Miley, G. K., Lub, J., & de, Jong, T., 1985, Nature, 314, 240
- di Serego Alighieri, S., Cimatti, A., Fosbury, R. A. E., & Hes, R., 1997, A&A, 328, 510
- Eracleous, M., & Halpern, J. P., 2003, ApJ, 599, 886
- Evans, I. N., 1988, ApJS, 67, 373

- Ferrarese, L., & Merritt, D., 2000, *ApJ*, 539, 9
- Gebhardt, K., Kormendy, J., Ho, L. C., et al. 2000, *ApJ*, 543, L5
- Grupe, D., Beuermann, K., Mannheim, K., & Thomas, H. -C., 1999, *A&A*, 350, 31
- Grupe, D., 2004, *AJ*, 127, 1799
- Gonzalez Delgado, R. M., Heckman, T., & Leitherer, C., 2001, *ApJ*, 546, 845
- Gonzalez Delgado, R. M., *ASPC*, 528, 101
- Granato, G. L., & Danese, L., 1994, *MNRAS*, 268, 235
- Granato, G. L., De Zotti, G. Silva, L., Bressan, A., & Danese, L., 2004, *ApJ*, 600, 580
- Hao, C. N., Xia, X. Y., Mao, S., Wu., Hong, & Deng, Z. G., 2005, *ApJ*, 625, 78
- Heckman, T. M., Kauffmann, G., Brinchmann, J., et al. 2004, *ApJ*, 613, 109
- Jackson, N., Browne, I. W. A., Murphy, D. W., & Saikia, D. J., 1989, *Nature*, 338, 485
- Joguet, B., Kunth, D., Melnick, J., Terlevich, R., & Terlevich, E., 2001, *A&A*, 380, 19
- Keel, W. C., de Grijp, M. H. K., Miley, G. K., & Zheng, W., 1994, *A&A*, 283, 791
- Kewley, L. J., Heisler, C. A., Dopita, M. A., & Lumsden, S., *ApJS*, 2001, 132, 37
- King, A. R., & Pounds, K. A., 2003, *MNRAS*, 345, 657
- Kriss, G., 1996, *Adass*, 3, 437
- Kuraszkiewicz, J., Wilkes, B. J., Brandt, W. N., et al. 2000, *ApJ*, 542, 631
- Kuraszkiewicz, J. K., Green, P. J., Crenshaw, D. M., Dunn, J., Forster, K., Vestergaard, M., Aldcroft, T. L., 2004, *ApJS*, 150, 165
- Laor, A., 2003, *ApJ*, 590, 86
- Laor, A., Fiore, F., Martin, E., et al. 1997, *ApJ*, 477, 93
- Lawrence, A., Elvis, M., Wilks, B. J., McHardy, I., & Brandt, N., 1997, *MNRAS*, 285, 879
- Lipari, S., 1994, *ApJ*, 436, 102
- Low, F. J., Huchra, J. P., Kleinmann, S. G., & Cutri, R. M., 1988, *ApJ*, 327, 41

- Magorrian, J., Tremaine, S., Richstone, D., et al. 1998, *AJ*, 115, 2285
- Marconi, A.; Hunt, L. K., 2003, *ApJ*, 589, 21
- Marziani, P., Sulentic, J. W., Dultzin-Hacyan, D., & Calvani, M., 2001, *ApJ*, 558, 553
- Marziani, P., Sulentic, J. W., Zamanov, R., & Calvani, M., 2003a *Mem. Soc. Astron. Italiana*, 74, 490
- Marziani, P., Zamanov, R., Sulentic, J. W., & Calvani, M., 2003b, *MNRAS*, 345, 1133
- Massey, P., Strobel, K., Barnes, J. V., & Anderson, E., 1988, *ApJ*, 328, 315
- Mathur, S., 2000, *MNRAS*, 314, L17
- Netzer, H., Shemmer, O., Maiolino, R., Oliva, E., Croom, S., Corbett, C., & di Fabrizio, L., 2004, *ApJ*, 614, 558
- Norman, C., & Scoville, N., 1988, *ApJ*, 332, 124
- O'Brien, P. T., Dietrich, M., Leighly, K., et al. 1998, *ApJ*, 509, 163
- Oke, J. B., & Lauer, T. R., 1979, *ApJ*, 230, 360
- Osterbrock, D. E., 1989, *Astrophysics of Gaseous Nebulae and Active Galactic Nuclei* (University Science Book: Mill Valley, CA)
- Phillips, M. M., 1978, *ApJ*, 226, 736
- Pier, E. A., & Krolik, J. H., 1992, *ApJ*, 401, 99
- Richstone, D., Ajhar, E. A., Bender, R., 1998, *Nature*, 395, A14
- Rodriguez-Ardila, A., Pastoriza, M. G., & Donzelli, C. J., 2000, *ApJS*, 126, 63
- Rodriguez-Ardila, A., & Viegas, S. M., 2003, *ApJ*, 340, 33
- Sanders, D. B., & Mirabel, I. F., 1996, *ARA&A*, 34, 749
- Sanders, D. B., Soifer, B. T., Elias, J. H., Madore, B. F., Matthews, K., Neugebauer, G., Scoville, N. Z., 1988, *ApJ*, 325, 74
- Stockton, A., & Ridgway, S. E., 1991, *AJ*, 102, 488
- Storey, P. J., & Zeppen, C. J., 2000, *MNRAS*, 312, 813

- Strateva, I. V., Strauss, M. A., Hao, L., et al. 2003, *AJ*, 126, 1720
- Sulentic, J. W., Marziani, P., & Dultzin-Hacyan, D., 2000a, *ARA&A*, 38, 521
- Sulentic, J. W., Zwitter, T., Marziani, P., & Dultzin-Hacyan, D., 2000b. *ApJ*, 536, 5
- Sulentic, J. W., Marziani, P., Zwitter, T., Dultzin-Hacyan, D., & Calvani, 2000c, *ApJ*, 545, 15
- Sulentic, J. W., Marziani, P., & Zamanov, R., et al. 2002, *ApJ*, 566, 71
- Sulentic, J. W., Stirpe, G. M., & Marziani, P., et al. 2004, *A&A*, 423, 121
- Tremaine, S., Gebhardt, K., Bender, R., et al. 2002, *ApJ*, 574, 740
- Vaughan, S., Edelson, R., Warwick, R. S., et al. 2001, *MNRAS*, 327, 673
- Veilleux, S., & Osterbrock, D. E., 1987, *ApJS*, 63, 259
- Veron-Cetty, M. P., Joly, M., & Veron-Cetty, P., 2004, *A&A*, 417, 515
- Veron-Cetty, M. P., & Veron, P., 2001, *A&A*, 374, 92
- Wang, T., Brinkmann, W., & Bergeron, J., 1996, *A&A*, 309, 81
- Wang, J., Wei, J. Y., & He, X. T., 2004, *ChJAA*, 4, 415
- Wang, J., Wei, J. Y., & He, X. T., 2005, *A&A*, 436, 417
- Winkler, H., 1992, *MNRAS*, 257, 677
- Witt, H. J., Czerny, B., Zycki, P. T., 1997, *MNRAS*, 286, 848
- Xu, D. W., Komossa, S., Wei, J. Y., Qian, Y., & Zheng, X. Z., 2003, *ApJ*, 590, 73
- Zamanov, R., & Marziani, P., 2002, *ApJ*, 571, 77
- Zamanov, R., Marziani, P., Sulentic, J. W., Calvani, M., Dultzin-Hacyan, D., & Bachev, R., 2002, *ApJ*, 576, 9
- Zuther, J., Eckart, A., Scharwachter, J., Krips, M., & Straubmeier, C., 2004, *A&A*, 414, 919
- Zhou, H., Wang, T., Dong, X., Wang, J., & Lu, H., 2005, *Mem. Soc. Astron. Italiana*, 76, 93
- Zheng, X. Z., Xia, X. Y., Mao, S., Wu, H., & Deng, Z. G., 2002, *AJ*, 124, 18

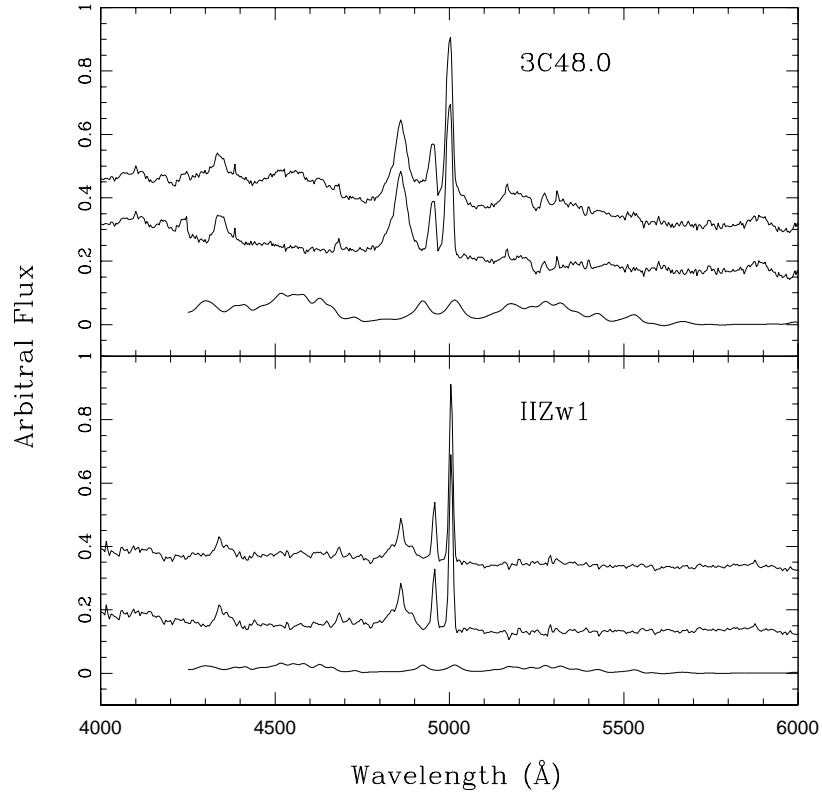


Fig. 1.— An illustration of the FeII subtraction in two typical cases, 3C 48.0 and II Zw 1. In each panel, the top curve is the observed spectrum which is shifted upward by an arbitrary amount for visibility. The middle curve is the FeII-subtracted spectrum, bottom curve the best adopted FeII template.

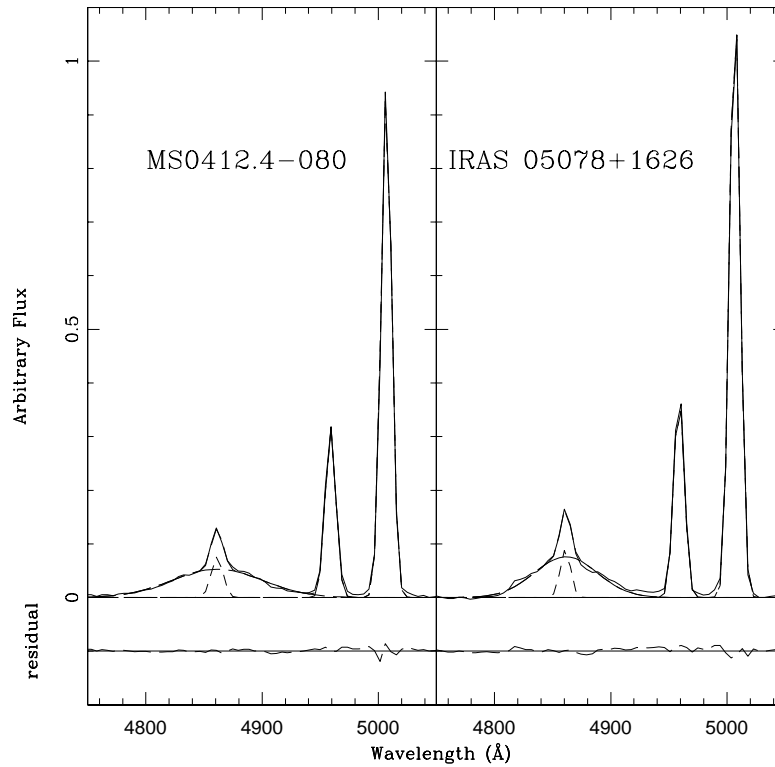


Fig. 2.— Profile modelling and decomposition for two typical objects, MS 0412.4-0802 and IRAS 05078+1626. The observed and modelled profiles are represented by light and heavy solid lines, respectively. The narrow peaks of $H\beta$ are displayed by short dashed lines for visibility, the broad $H\beta$ components by long dashed lines. The lower sub-panel underneath each spectrum illustrates the residuals between the observed and fitted emission profile.

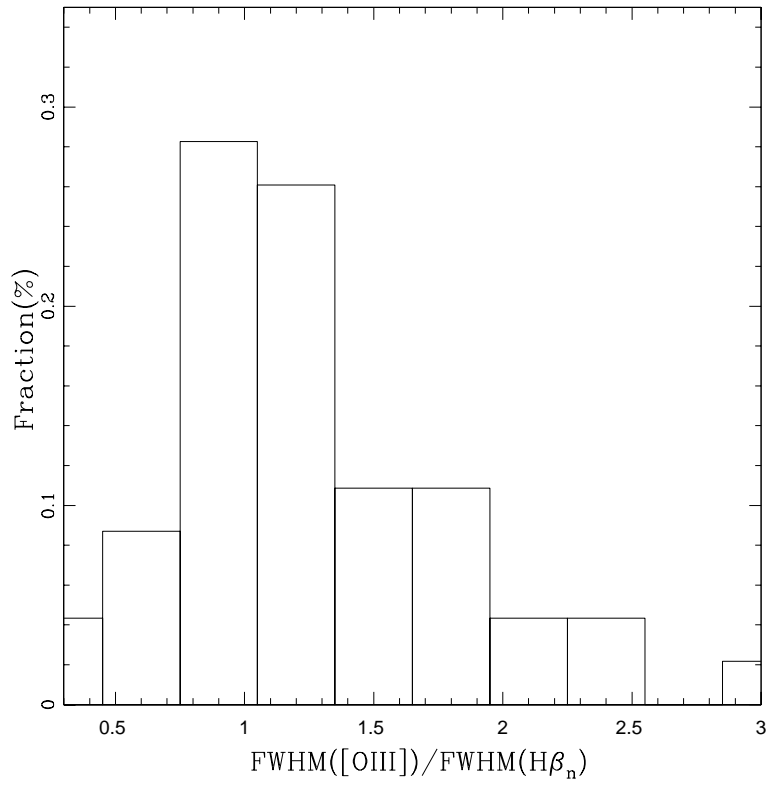


Fig. 3.— The fraction of the ratio of FWHM(Hβ) and FWHM([OIII]).

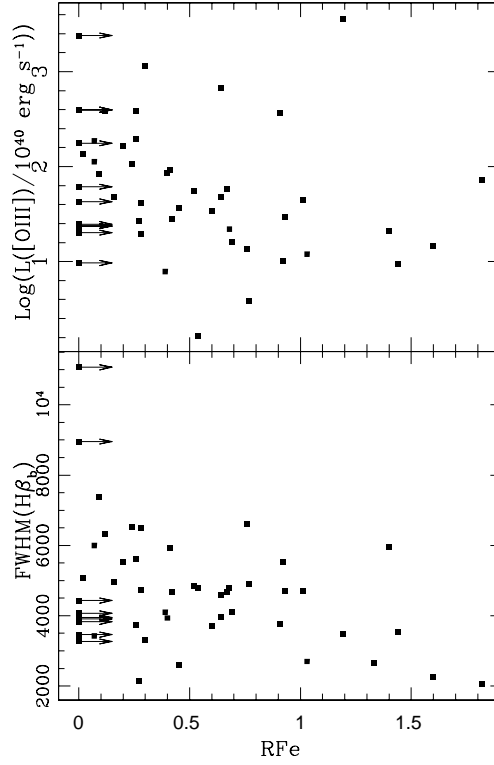


Fig. 4.— *Lower panel:* RFe plotted against the FWHM of $H\beta_b$ for all the object in our sample ($r_s = -0.321, P_s = 0.0279$). *Upper panel:* Plot of RFe vs. $L([OIII])$ ($r_s = -0.386, P_s = 0.0081$). In both panels, the points with zero fluxes of FeII are indicated by superposed arrows.

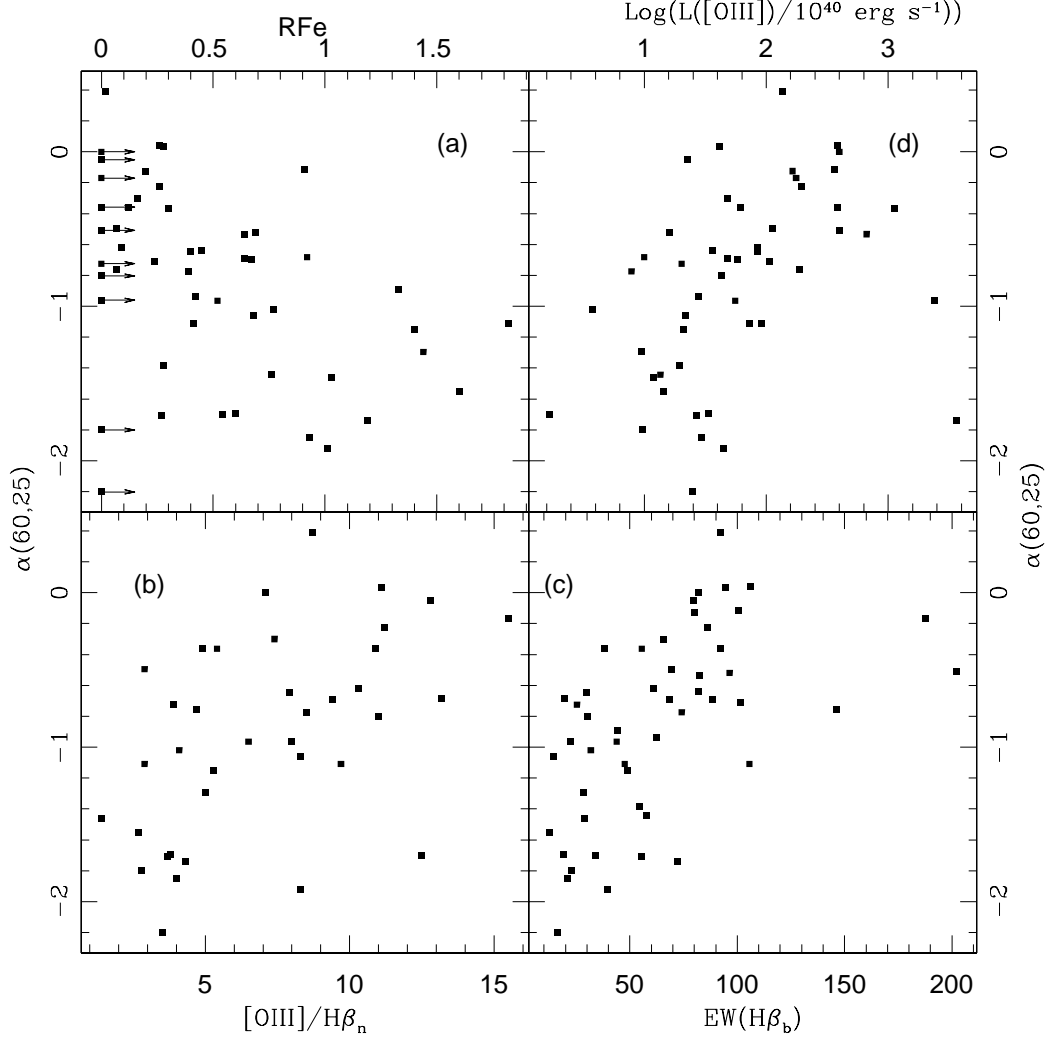


Fig. 5.— (a): Plot of mid-infrared color $\alpha(60,25)$ vs. R_{Fe} ($r_s=-0.518, P_s = 0.0003$). The correlation coefficient is calculated by survival analysis, because the data with zero FeII flux is nondetectable and considered to be lower limit of its true value. The points with zero fluxes of FeII are indicated by superposed arrows. (b): Mid-infrared color $\alpha(60,25)$ plotted against flux ratio $[OIII]/H\beta_n$ ($r_s=0.538, P_s = 0.0012$). (c): Mid-infrared color $\alpha(60,25)$ plotted against equivalent width of $H\beta$ broad component ($r_s=0.590, P_s < 10^{-4}$). (d): $L([OIII])$ plotted against $\alpha(60,25)$ ($r_s = 0.478, P_s = 0.0009$).

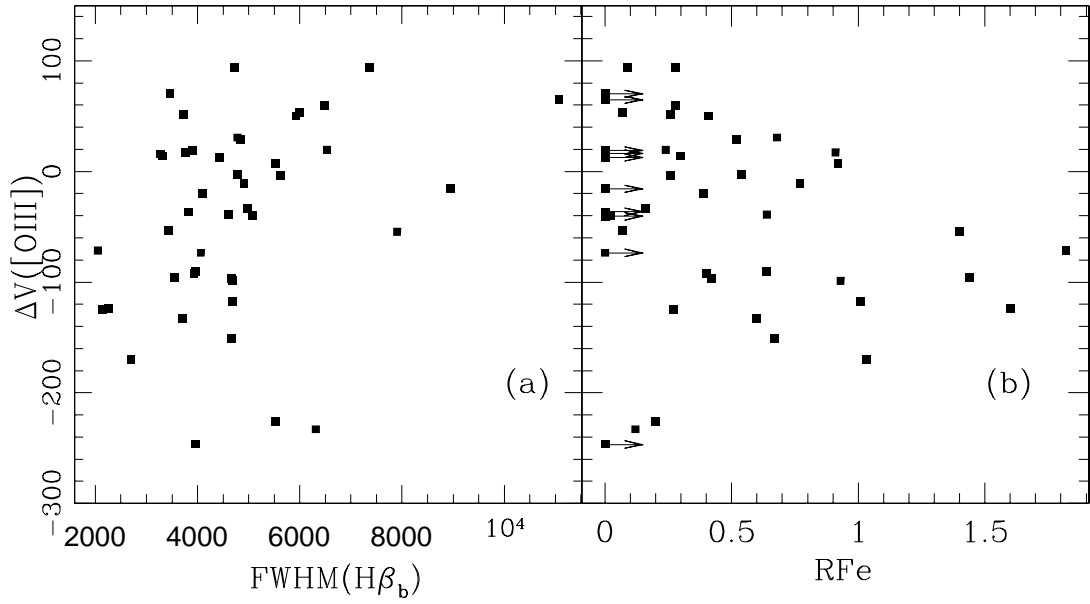


Fig. 6.— (a) $\text{FWHM}(\text{H}\beta_b)$ plotted against the velocity shift of $[\text{OIII}]$ with respect to the peak of $\text{H}\beta$ narrow component, $\Delta V([\text{OIII}])$ ($r_s = -0.343$, $P_s = 0.0230$). (b): The RFe plotted against $\Delta V([\text{OIII}])$ ($r_s = -0.320$, $P_s = 0.0319$). The survival analysis is carried out to replace the ordinary Spearman rank-order analysis. The points considered to be lower limits of RFe are indicated by arrows.

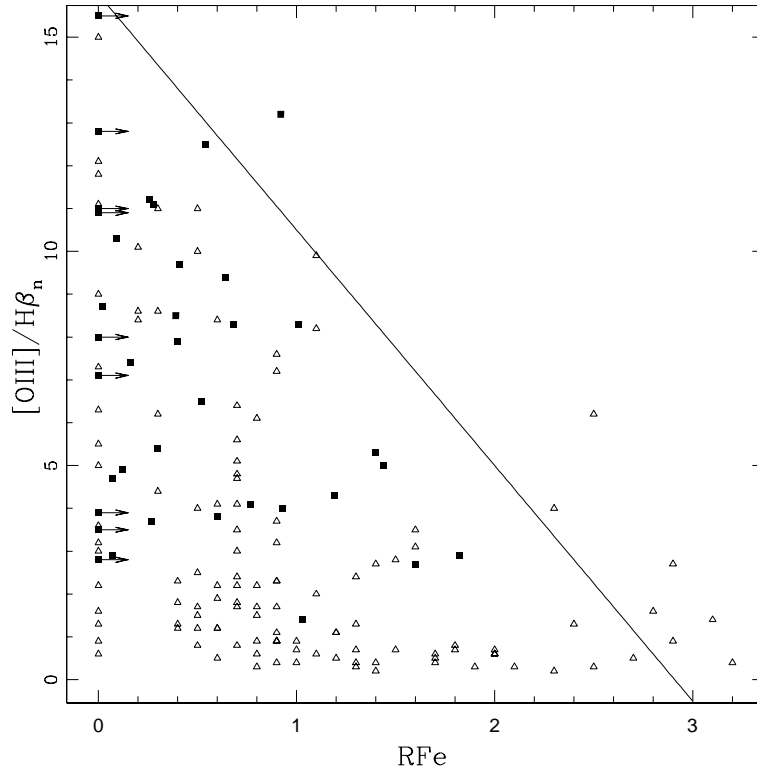


Fig. 7.— RFe plotted against the flux ratio $[OIII]/H\beta_n$ ($r_s=-0.252$) for 36 out of 50 objects in our sample and for data in Xu et al. (2003). Our sample is denoted by solid square, and sample of Xu et al. (2003) by open triangle. The superposed arrows indicate that the corresponding values of the RFe is the lower limits. The solid line from left-top to right-bottom indicates the position of the envelope drawn by eye.

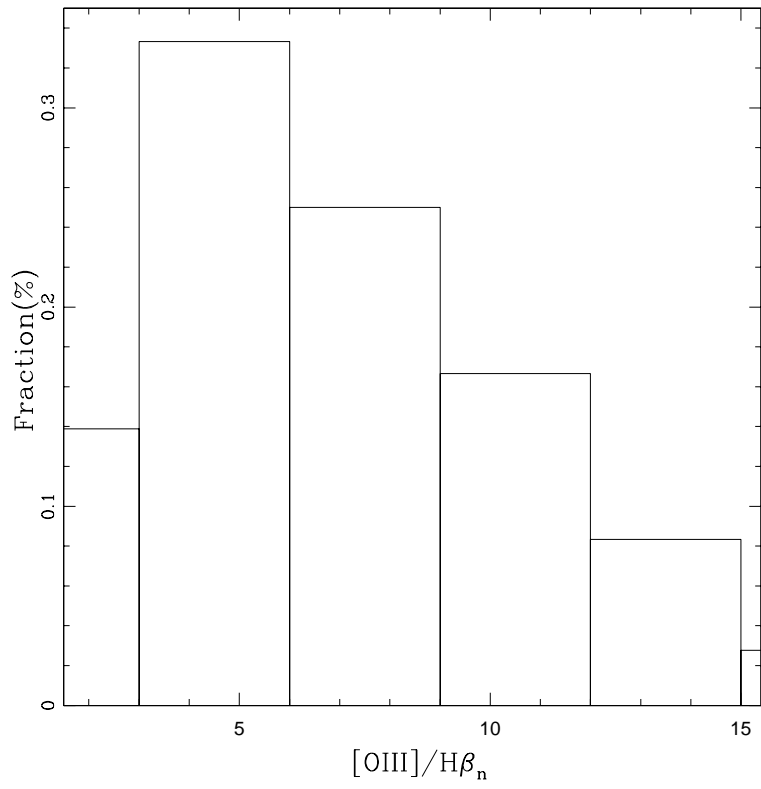


Fig. 8.— Distribution of line flux ratio $[\text{OIII}]/\text{H}\beta_n$ for 36 objects with determined $\text{H}\beta$ narrow component in our sample.

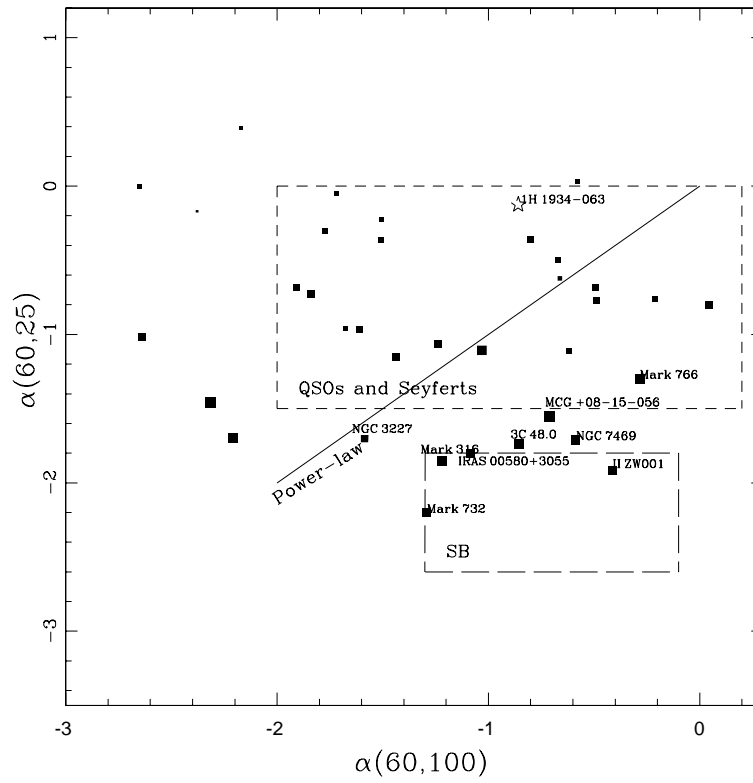


Fig. 9.— IRAS color-color diagram. The localizations of AGN and starburst regions are displayed by short and long dashed lines, respectively. The size of each point is proportional to the projection on Eigenvector 1 of that object.

Table 1. Log of Spectroscopic Observation

Object name (1)	Set (2)	R.A. (3)	Dec (4)	z (5)	Date (6)	Exp (7)	m _v (8)	M _B (9)	AGN Type (10)
Mark 543	B	000226.4	+032106	0.025518	2004 Sep 17	1200	14.68	-20.6	S1.5
IRAS 00580+3055	A	010048.0	+311200	0.051100	2001 Nov 19	1800	15.80	-21.6	S1.5
II Zw001	A	012159.8	-010224	0.054341	2001 Nov 17	1500	15.17	-21.8	S1.5
3C 48.0	A	013741.3	+330935	0.367000	2001 Nov 19	2100	16.20	-25.2	QSO S1.5
NGC 985	A	023437.8	-084715	0.043143	2001 Oct 12	1800	14.28	-22.4	S1.5
NGC 1019	A	023827.4	+015428	0.024187	2001 Nov 17	2000	14.95	-20.1	S1.5
NGC 1275	A	031948.2	+413042	0.017559	2001 Nov 17	900	12.48	-21.9	S1.5
MS 0412.4-0802	A	041452.7	-075540	0.037910	2001 Oct 12	1500	14.91	-21.1	S1.5
3C 120	A	043311.1	+052116	0.033010	2001 Nov 17	1600	15.05	-20.8	S1.5
NPM1G -05.0216	A	044720.7	-050814	0.044200	2001 Nov 19	1500	15.11	-21.2	S1.5
IRAS 05078+1626	A	051045.5	+162956	0.017880	2001 Nov 17	2000	15.64	-19.4	S1.5
MCG +08-11-011	A	055453.6	+462621	0.020484	2001 Nov 16	1200	14.62	-20.0	S1.5
Mark 6	A	065212.3	+742538	0.018813	2001 Nov 16	1200	14.19	-20.1	S1.5
Mark 376	A	071415.1	+454156	0.055980	2001 Nov 18	1650	14.62	-22.5	S1.5
IRAS F07144+4410	A	071800.6	+440527	0.061440	2001 Nov 16	1500	15.50	-22.3	S1.5
Mark 9	A	073657.0	+584613	0.039874	2001 Nov 18	1000	14.37	-22.1	S1.5
B3 0754+394	A	075800.1	+392029	0.096000	2001 Dec 17	1800	14.36	-24.1	QSO S1.5
MCG +08-15-056	A	081516.8	+460430	0.040975	2001 Nov 19	1500	15.20	-21.7	S1.5
NGC 3227	A	102330.6	+195156	0.003860	2001 Nov 18	600	11.79	-18.7	S1.5
NGC 3516	A	110647.4	+723407	0.008840	2001 Nov 19	500	12.40	-20.5	S1.5
Mark 732	A	111349.8	+093510	0.029230	2004 May 21	1050	14.17	-21.4	S1.5
Mark 1447	A	113029.1	+493458	0.095900	2002 Feb 12	2400	16.00	-22.8	S1.5
Mark 766	A	121826.7	+294847	0.012930	2002 Feb 11	1200	13.57	-20.0	S1.5
Mark 1320	A	121908.8	-014829	0.103000	2002 Feb 13	1800	15.00	-24.0	QSO S1.5
PG 1351+640	A	135315.7	+634546	0.088200	2004 May 22	2700	14.28	-24.1	QSO S1.5
Mark 662	A	135406.4	+232549	0.055000	2002 Feb 11	1800	15.37	-21.6	S1.5
CSO 409	A	140438.8	+432707	0.323300	2002 Feb 15	2000	15.62	-25.9	QSO S1.5
OQ 208	A	140700.4	+282715	0.076576	2002 Feb 12	1650	15.35	-22.2	S1.5
NGC 5548	A	141759.5	+250812	0.017175	2004 May 21	1200	13.73	-20.7	S1.5
H 1419+480	B	142129.8	+474725	0.072296	2003 Feb 02	3000	15.40	-22.8	S1.5
CGCG 163-074	A	143209.0	+313505	0.055108	2002 Feb 13	1650	15.50	-22.1	S1.5
Mark 817	A	143622.1	+584739	0.031455	2002 Feb 14	1200	13.79	-22.3	S1.5
Mark 841	A	150401.2	+102616	0.036422	2002 Feb 11	1500	14.27	-22.2	S1.5
SBS 1527+564	A	152907.5	+561605	0.099000	2002 Feb 14	2100	15.80	-23.1	QSO S1.5

Table 1—Continued

Object name (1)	Set (2)	R.A. (3)	Dec (4)	z (5)	Date (6)	Exp (7)	m _v (8)	M _B (9)	AGN Type (10)
Mark 290	A	153552.3	+575409	0.029577	2002 Feb 13	1800	14.96	-20.7	S1.5
Mark 871	A	160836.4	+121951	0.033657	2002 Feb 15	2100	14.94	-20.9	S1.5
TON 0256	A	161413.2	+260416	0.131000	2004 May 22	3000	15.41	-23.5	QSO S1.5
3C 351	A	170441.5	+604428	0.371940	2002 Feb 14	2200	15.28	-26.5	QSO S1.5
UGC 10683B	A	170500.4	-013230	0.032000	2004 May 23	2400	15.55	-19.5	S1.5
RX J1715.9+3112	A	171602.0	+311223	0.111000	2004 May 22	3600	16.00	-23.2	QSO S1.5
IRAS 17216+3633	A	172323.3	+363010	0.040000	2004 May 21	3600	16.00	-20.9	S1.5
3C 390.3	A	184209.0	+794617	0.056100	2003 Oct 25	3600	15.38	-21.6	S1.5
1H 1934-063	A	193733.2	-061306	0.010587	2001 Sep 21	1200	15.35	-17.8	S1.5
Mark 509	B	204409.7	-104324	0.034397	2004 Sep 17	2400	13.12	-23.3	QSO S1.5
3C 445.0	A	222349.7	-020613	0.056200	2001 Nov 17	1500	15.77	-20.8	S1.5
MR 2251-178	A	225405.9	-173455	0.063980	2001 Nov 19	900	14.36	-23.1	QSO S1.5
NGC 7469	A	230315.6	+085226	0.016317	2001 Sep 21	600	13.04	-21.6	S1.5
Mark 315	A	230402.7	+223727	0.038870	2001 Nov 17	1200	14.78	-21.3	S1.5
Mark 316	A	231340.5	+140115	0.040902	2001 Nov 18	1200	15.20	-21.7	S1.5
NGC 7603	A	231856.6	+001438	0.029524	2001 Nov 18	1000	14.01	-21.5	S1.5

Note. — Col.(1), Object name. Col.(2), Set of spectra described in the text. Col.(3), Object's right ascension. Col.(4), Declination of object. Col.(5), Redshift from NED. Col.(6), Date of observation. Col.(7), Averaged exposure time in seconds. Col.(8), apparent magnitude in V band. Col.(9), Absolute magnitude at B band from Veron-Cetty & Veron(2001). Col.(10), Classification type of AGN

Table 2. List of Emission Line Properties

Name	H β_n EW(Å)	H β_b EW(Å)	FeII EW(Å)	RFe	H β_n FWHM ^a	H β_b FWHM ^a	[OIII] FWHM ^a	[OIII]/H β_n	$\Delta V(H\beta_b)$ ^b (km s ⁻¹)	$\Delta V([OIII])$ ^c (km s ⁻¹)	$\alpha(100, 60)$	$\alpha(60, 25)$	$\log(\frac{L([OIII])}{10^{40} \text{ erg s}^{-1}})$
(1)	(2)	(3)	(4)	(5)	(6)	(7)	(8)	(9)	(10)	(11)	(12)	(13)	(14)
Mark 543	3.6	25.4	0.0	0.00	264.0	3827.8	256.5	3.9	-25.9	-36.4	-1.841	-0.724	1.305
IRAS 00580+3055	9.0	22.7	0.0	0.00	656.7	3460.3	515.1	2.8	-165.0	70.2	-1.084	-1.800	0.985
II Zw001	6.3	39.6	39.8	1.01	499.3	4693.4	545.2	8.3	-184.4	-117.4	-0.413	-1.918	1.649
3C 48.0	11.2	72.1	85.6	1.19	1361.8	3473.2	1087.9	4.3	-275.5	-444.1	-0.856	-1.739	3.558
NGC 985	6.5	105.6	43.0	0.41	617.9	5933.2	597.5	9.7	-9.4	49.9	-0.617	-1.109	1.962
NGC 1019	5.1	31.8	24.6	0.77	584.8	4914.6	372.6	4.1	-297.5	-11.0	-2.637	-1.019	0.579
NGC 1275	10.3	30.1	0.0	0.00	502.3	3950.2	1654.7	11.0	-62.5	-246.7	0.046	-0.803	1.632
MS0412.4-0802	16.2	86.3	22.7	0.26	539.1	5618.8	406.1	11.2	17.9	-3.8	-1.506	-0.224	2.287
3C 120	101.6	23.9	0.24	1443.6	6530.0	686.2	783.4	19.6	-1.358	-0.711	2.029
NPM1G-05.0216	9.2	29.1	30.0	1.03	426.9	2699.0	693.2	1.4	169.1	-169.6	-2.317	-1.458	1.077
IRAS 05078+1626	15.3	79.4	0.0	0.00	330.1	3904.1	308.4	12.8	26.5	19.1	-1.718	-0.052	1.357
MCG +08-11-011	38.1	69.2	4.9	0.07	1416.3	6001.5	820.2	2.9	922.1	53.2	-0.672	-0.495	2.051
Mark 6	15.3	60.8	5.7	0.09	894.7	7374.8	1014.7	10.3	-350.2	93.6	-0.661	-0.621	1.927
Mark 376	96.5	67.0	0.69	4094.0	542.7	-1.054	-0.520	1.209
IRAS F07144+4410	106.2	27.1	0.26	1450.7	3733.8	957.3	-467.1	52.1	-2.881	0.039	2.581
Mark 9	81.8	36.9	0.45	2582.5	715.9	-0.688	-0.638	1.562
B3 0754+394	82.3	52.8	0.64	1580.3	4599.7	644.6	-165.9	-38.8	-2.781	-0.533	2.824
MCG +08-15-056	8.5	12.4	19.8	1.60	626.3	2247.0	571.3	2.7	64.2	-124.0	-0.712	-1.553	1.160
NGC 3227	5.2	33.9	18.3	0.54	612.2	4778.9	746.4	12.5	-332.5	-2.9	-1.586	-1.702	0.220
NGC 3516	2.7	74.2	29.1	0.39	634.5	4101.6	591.7	8.5	-198.0	-19.7	-0.491	-0.773	0.896
Mark 732	3.8	16.2	0.0	0.00	872.7	4427.9	686.9	3.5	226.5	12.7	-1.292	-2.201	1.394
Mark 1447	2.4	48.8	68.5	1.40	645.0	7902.7	815.3	5.3	-1145.3	-54.4	-1.436	-1.150	1.319
Mark 766	22.9	28.7	41.3	1.44	830.5	3544.9	428.2	5.0	-302.2	-95.5	-0.285	-1.296	0.978
Mark 1320	6.9	30.0	12.0	0.40	565.8	3934.7	409.3	7.9	-613.3	-91.8	-3.474	-0.646	1.929
PG 1351+640	7.2	38.4	4.4	0.12	707.8	6316.1	986.4	4.9	-18.3	-233.0	-0.799	-0.358	2.581
Mark 662	1.0	19.3	17.7	0.92	417.8	5536.8	782.9	13.2	40.2	7.8	-1.908	-0.683	1.000
CSO409 ^d	44.4	59.2	1.33	2641.0	-0.918	-0.889
OQ 208	2.1	68.5	43.9	0.64	326.5	3951.1	764.1	9.4	1719.6	-90.1	-0.493	-0.687	1.679
NGC 5548	10.5	92.5	0.0	0.00	556.6	609.0	10.9	-40.5	-0.997	-0.358	1.789
H 1419+480	80.1	16.4	0.20	1006.0	5531.4	541.4	-239.6	-226.3	-0.859	-0.125	2.217
CGCG 163-074	3.3	14.6	10.0	0.68	878.4	4779.2	699.3	8.3	-24.7	30.7	-1.241	-1.062	1.340
Mark 817	88.5	59.3	0.67	1618.0	4661.3	663.3	13.7	-150.4	-0.034	-0.694	1.765
Mark 841	3.4	94.3	26.7	0.28	723.7	6485.2	773.6	11.1	-145.4	59.7	-0.580	0.033	1.613

Table 2—Continued

Name	H β_n EW(Å)	H β_b EW(Å)	FeII EW(Å)	RFe	H β_n FWHM ^a	H β_b FWHM ^a	[OIII] FWHM ^a	[OIII]/H β_n	$\Delta V(H\beta_b)$ ^b (km s ⁻¹)	$\Delta V([OIII])$ ^c (km s ⁻¹)	$\alpha(100, 60)$	$\alpha(60, 25)$	$\log(\frac{L([OIII])}{10^{40} \text{ erg s}^{-1}})$
(1)	(2)	(3)	(4)	(5)	(6)	(7)	(8)	(9)	(10)	(11)	(12)	(13)	(14)
SBS 1527+564	20.7	82.1	0.0	0.00	480.5	4064.7	586.5	7.1	69.0	-73.5	-2.652	0.000	2.599
Mark 290	5.8	65.7	10.6	0.16	487.2	4972.4	482.3	7.4	-37.8	-33.6	-1.773	-0.300	1.682
Mark 871	62.5	26.1	0.42	475.3	4670.4	328.5	-58.8	-96.9	-0.432	-0.937	1.447
TON 0256	15.4	55.5	16.6	0.30	798.2	3307.6	479.3	5.4	43.3	14.3	-1.510	-0.364	3.056
3C 351.0	3.2	22.2	0.0	0.00	692.4	8957.4	508.9	8.0	64.0	-15.6	-1.677	-0.961	3.381
UGC 10683B	54.7	15.2	0.28	1069.2	4721.9	616.3	29.2	93.7	-3.525	-1.384	1.286
RX J1715.9+3112	100.5	91.3	0.91	1376.6	3772.9	440.4	79.6	17.4	-3.095	-0.118	2.560
IRAS 17216+3633	13.8	43.9	22.6	0.52	681.0	4837.4	540.9	6.5	-50.4	29.2	-1.609	-0.964	1.747
3C 390.3	5.0	92.5	1.9	0.02	647.4	5070.7	600.8	8.7	-4071.9	-39.3	-2.169	0.393	2.130
1H 1934-063	80.1	16.4	0.20	1006.0	5531.4	541.4	-239.6	-226.3	-0.859	-0.125	1.861
Mark 509	9.5	146.1	10.4	0.07	567.4	3428.8	466.1	4.7	56.9	-53.4	-0.213	-0.759	2.270
3C 445.0	11.9	187.7	0.0	0.00	451.6	3269.7	531.6	15.5	-418.0	16.1	-2.379	-0.170	2.245
MR 2251-178	202.0	0.0	0.00	2089.7	11067.5	938.7	247.7	64.7	-1.316	-0.508	2.599
NGC 7469	11.3	55.3	14.9	0.27	784.2	2140.1	875.6	3.7	42.2	-124.7	-0.586	-1.710	1.427
Mark 315	8.0	18.9	11.4	0.60	428.1	3699.5	725.0	3.8	-15.3	-133.2	-2.209	-1.696	1.529
Mark 316	12.6	21.1	19.5	0.93	558.8	4689.0	607.6	4.0	60.4	-98.9	-1.222	-1.850	1.470
NGC 7603	57.5	43.5	0.76	6597.9	856.0	-1.706	-1.443	1.133

^aIn units of km s⁻¹^bH β broad component velocity shifts with respect to narrow component. A positive velocity indicates a redshift of H β_b with respect to H β_n , and a negative velocity a blueshift of H β_b .^c[OIII] velocity shifts with respect to narrow component of H β . A redshift of [OIII] is indicated by a positive velocity, and a blueshift by a negative velocity.^dThe source shows not detectable [OIII] λ 5007 emission line.

Table 3. Spearman Rank-Order Correlation Coefficient Matrix

Property	EW($H\beta_b$) (1)	EW(FeII) (2)	RFe (3)	FWHM($H\beta_b$) (4)	[OIII]/ $H\beta_n$ (5)	$\Delta V(H\beta_b)$ (6)	$\Delta V([OIII])$ (7)	$\alpha(60,100)$ (8)	$\alpha(60,25)$ (9)	$\log(L([OIII]))$ (10)
(1)EW($H\beta_b$)	0.272	-0.334(0.0206)	0.112	0.429(0.0111)	-0.032	0.257	0.042	0.590(0.0000)	0.522(0.003)
(2)EW(FeII)	0.692(0.000)	-0.185	-0.025	-0.087	0.159	-0.081	-0.140	-0.064
(3)RFe	-0.298	-0.252	0.004	-0.320(0.0319)	-0.027	-0.518(0.0003)	-0.386(0.0081)
(4)FWHM($H\beta_b$)	0.425(0.0120)	-0.018	0.343(0.0230)	-0.020	0.259	0.109
(5)[OIII]/ $H\beta_n$	-0.331(0.050)	0.341(0.0408)	-0.006	0.538(0.0012)	0.137
(6) $\Delta V(H\beta_b)$	0.069	0.059	-0.039	0.124
(7) $\Delta V([OIII])$	-0.286	0.248	0.006
(8) $\alpha(60,100)$	-0.210	-0.098
(9) $\alpha(60,25)$	0.478(0.0009)
(10) $\log(L([OIII]))$

Table 4: Correlations of eigenvectors with line and continuum properties

Property	Eigenvector 1	Eigenvector 2	Eigenvector 3	Eigenvector 4
Eigenvalue	3.055	1.444	1.185	1.040
Cumulative	33.9%	49.9%	63.2%	74.7%
EW($H\beta_b$) ...	-0.709	-0.230	-0.476	0.888
RFe	0.643	0.302	-0.353	0.162
FWHM($H\beta_b$)	-0.537	0.386	0.108	-0.354
[OIII]/ $H\beta_n$..	-0.712	0.391	-0.204	0.037
$\Delta V(H\beta_b)$	0.174	-0.667	0.380	-0.442
$\Delta V([OIII])$..	-0.557	0.358	0.364	-0.393
$\alpha(100,60)$	0.134	-0.076	-0.679	-0.681
$\alpha(60,25)$	-0.841	-0.145	0.082	0.224
$\log(L([OIII]))$	-0.527	-0.638	-0.188	0.128